Silver-Atom Modulation of Ti Vacancies in MXene Enables Uniform Spherical Lithium Deposition

Xue Liang Li[1], Wei Ying Lieu[1,2], Liguang Wang[3], Dong Yan[4], Yifan Li[1], Tanmay Ghosh[2], Yuanjian Li[2], Jun Lu[3]*, Zhi Wei Seh[2]*, Hui Ying Yang[1]*

[1]Singapore University of Technology and Design, Pillar of Engineering Product Development, 8 Somapah Road, Singapore 487372, Republic of Singapore

[2]Institute of Materials Research and Engineering (IMRE), Agency for Science, Technology and Research (A*STAR), 2 Fusionopolis Way, Innovis #08-03, Singapore 138634, Republic of Singapore

[3]College of Chemical and Biological Engineering, Zhejiang University, Hangzhou, Zhejiang, 310027, China

[4]International Joint Laboratory of New Energy Materials and Devices of Henan Province, School of Physics & Electronics, Henan University, Kaifeng, Henan, 475004, China

*Corresponding authors: junzoelu@zju.edu.cn; sehzw@imre.a-star.edu.sg; yanghuiying@sutd.edu.sg

Abstract: Effective management of lithium (Li) metal nucleation and growth is critical for its practical application, yet limited understanding of Li metal anode morphology has impeded progress. This study advances the comprehension of dense spherical Li deposition by linking atomic charge distributions to macroscopic phenomena. By introducing silver (Ag) single atoms into titanium (Ti) vacancies in MXene, we form a unique Ag-C composite that modulates charge distribution, thereby facilitating uniform, spherical Li deposition across the surface. This approach minimizes Ag consumption to below 1 wt% while achieving Li metal deposition capacities exceeding 40 mAh cm^{-2}. Moreover, full cells incorporating MXene-AgSAs@Li anodes paired with $LiFePO_4$ or sulfur cathodes exhibit significantly enhanced cycling performance and high-rate capabilities. These findings provide novel insights into the role of charge partitioning in Li metal deposition and the formation of dense, spherical Li arrays.

The ongoing quest for clean and renewable energy has resulted in a growing demand for the development of efficient energy storage devices.[1-3] Lithium-ion batteries (LIBs) have been widely used in everyday life due to their safety and long lifespan.[4-8] However, the energy densities of current LIBs are nearly approaching their theoretical limits and are insufficient to meet the growing demands for advanced energy storage devices. Lithium (Li) metal anode, with a high specific capacity (3860 mAh g^{-1}) and a low redox potential (-3.04 V vs. standard hydrogen electrode), is regarded as one of the most promising anode materials.[9-11] Therefore, Li-sulfur and Li-air batteries, which are based on the Li metal anode, have been extensively investigated in the past decades for the construction of high-energy density batteries.[12-16]

Although Li metal batteries have received a great amount of attention, there are a series of issues associated with their practical application. One of the most critical issues is the formation of Li dendrites.[17-19] Li dendrites are Li crystals produced by the irregular electrodeposition of highly reactive Li atoms at the interface between the nucleation site and the solid electrolyte interface (SEI) film.[20-22] Such small and slender Li dendrites tend to break and lose their electrical contact with the bulk Li, subsequently forming "dead Li", leading to severe capacity loss.[23, 24] In addition, the formation of Li dendrites not only deteriorates battery performance but also leads to thermal runaway due to internal short circuits, posing serious safety hazards.[25, 26] Therefore, controlling the nucleation and growth of Li metal and inhibiting the growth of Li dendrites is the key to achieving the next generation of high energy density and safe Li metal batteries. Deep plating and stripping of Li represent significant challenges, heavily influenced by the initial nucleation of Li. Consequently, the control of Li nucleation and early growth on specialized substrates also emerges as a crucial factor in enhancing recyclability. As demonstrated in a prior investigation, the swift diffusion of Li at the interfaces of Li/solid electrolyte interphase (SEI) and Li/substrate enables rapid "self-rearrangement", facilitating early nucleation and resulting in a more uniform Li growth profile.[27, 28] Regarding substrate effects, it was also observed that a high affinity with the substrate material facilitated Li deposition. To understand deeply, metals capable

of alloy formation (e.g., silver and gold) are frequently employed to lower barriers to Li deposition. For example, Cui's team proposed that hollow carbon spheres modified with Au nanoparticles effectively promoted Li deposition and obstructed the formation of Li dendrites.[29] Lou's group also revealed that carbon fibers doped with nitrogen can be implanted with Ag nanoparticles to create a stable Li anode.[30] These reports illustrate that Au or Ag metals have an important role to play in the field of LMBs. However, their high prices and unclear essential cause of lithiophilicity limit their practical application in LMBs, resulting in the necessity to investigate the mechanism of Li deposition to design better Li dendrite inhibiting strategies.

Controlling the initial phase of Li growth is crucial to minimize both Li dendrite formation and high-capacity deposition. Several studies have found that the growth of Li dendrites can be inhibited by regulating the formation of spherical Li.[31, 32] To investigate the underlying reasons for the formation of spherical Li, we try to introduce Ag single atoms into the titanium (Ti) vacancies of MXene, a two-dimensional material with excellent electrical conductivity. As we know, the successful introduction of Pt and Ni single atoms into the Ti vacancies of MXene has been reported.[33, 34] However, introducing single atoms into Ti vacancies presents challenges, as metal single atoms may bind to the oxygen termination group of MXene instead of occupying the Ti vacancy.[35] Particularly, the incorporation of Ag single atoms remains relatively unexplored due to the high reactivity of Ag^+ ions, which form Ag particles easily in the presence of the highly oxidizing MXene. As a result, there are few reports regarding the introduction of Ag single atoms into Ti vacancies. In this work, Ag single atoms were used to occupy the Ti vacancies as the atomic radius of Ag (144 pm) is close to that of Ti (147 pm), likely enabling better compatibility. Experimentally, we observed that the Ag single atoms have successfully occupied the Ti vacancies, bringing upon the extra benefit of cost affordability. In addition, this study also contributes a novel aspect by reporting on the Ag-C system, which has been scarcely explored in previous studies on Ag single atoms as existing studies on Ag single atoms are mainly based on the Ag-O and Ag-N systems.[36, 37] Coupled with our novel synthesis method that

effectively reduces reaction rate through an inhibitive solvent, we can precisely deposit Ag single atoms in Ti vacancies.[23, 34] ensuring that the unique Ag-C system is showcased in our material, thus allowing our work to be a representative work for future researchers working to explore the Ag-C systems of Ag single atoms. Unlike conventional lithiophilic precious metal nanoparticles, the Ag single atoms are not only substantially cheaper (Table S1), but also have largely homogeneous morphological and atomistic characteristics, ensuring that the lithiophilic capability of each metal single atom site is consistent.[38-42] Furthermore, the introduction of Ag atoms into the Ti vacancies substantially homogenized the electronic environment near the Ti vacancies. This signifies the impact of charge modifications on Li deposition from an atomic-level viewpoint for the first time, offering a deeper comprehension of the effect of macroscopic charge distribution on Li deposition.

As a result, we utilize Ag single atoms to form uniform electronic sites that can modulate current densities and induce homogeneous spherical Li metal deposition, allowing dense and uniform spherical Li metal to be formed in the initial deposition stage. This initial formation of spherical Li metal is observed to effectively inhibit the growth of Li dendrites even after depositing ultra-high capacity. Therefore, the Ag single atoms modified MXene electrodes show a low overpotential and high CE over 800 cycles, as well as deep plating-stripping capacities of up to 40 mAh cm^{-2}. COMSOL Multiphysics simulations also illustrate a more uniform deposition and distribution of electrons on the MXene-AgSAs electrode compared to MXene and Cu electrodes. This observation suggests a substantial role for Ag single atoms in modulating electronic behavior and impeding the growth of Li dendrites. To further demonstrate its practicality, the full cell of MXene-AgSAs@Li anode is assembled with $LiFePO_4$ and S respectively, which demonstrated a stable cycle life of over 400 (1C) and 1000 cycles (2C) respectively.

The MXene-AgSAs were synthesized via a facile vacancy capture-reduction method.[33, 34] As illustrated in Scheme S1 (Supporting Information), $Ti_3C_2T_x$ (MXene) sheets were obtained by etching Al from Ti_3AlC_2 with the assistance of LiF and HCl.

Afterwards, MXene was reacted with $AgNO_3$ in ethanol to conduct Ag^+ ion trapping and reduction (synthesis details in SI). The strongest powder X-ray diffraction (XRD) peak of Ti_3AlC_2 near 40° is observed to have disappeared after etching (Figure S1a) along with the formation of the main characteristic (002) peak of $Ti_3C_2T_x$, indicating the successful synthesis of MXene sheets (Figure S1b). Despite the thereafter introduction of silver atoms, diffraction peaks of Ag species are not observed, indicating the lack of crystalline Ag in the MXene-AgSAs sample. Nonetheless, inductively coupled plasma optical emission spectroscopy (ICP-OES) still indicates that the Ag content in MXene-AgSAs is 0.76 wt% (Table S2), serving as a preliminary suggestion that Ag may be present in MXene as single atoms. Scanning electron microscope (SEM) and transmission electron microscope (TEM) images of MXene show a typical layered structure with smooth surfaces (Figures S2 and S3), a characteristic which was retained after Ag incorporation (Figures S4 and S5). Further elemental mapping also revealed that there was no aggregation of Ag in the MXene-AgSAs sample. Moreover, the scanning transmission electron microscopy (STEM) image of the MXene-AgSAs and related elemental mapping images also demonstrate the uniform distribution of the Ag single atoms (Figure S6).

To study the status of Ag in MXene, X-ray absorption spectroscopy (XAS) measurements are performed at the Ag K-edge. The X-ray absorption near-edge structure (XANES) region of the XAS reveals that the energy edge of Ag in MXene-AgSAs is higher than that of Ag foil, indicating the Ag atoms in MXene-AgSAs are positively charged (Figure 1a). Further structural information of Ag single atoms can be obtained from Ag K-edge extended X-ray absorption fine structure (EXAFS) analyses. The Fourier-transformed R-space curves of the Ag K_3-edge EXAFS spectra unveiled the bonding environment of Ag atoms in MXene-AgSAs. As shown in Figure 1b, the MXene-AgSAs shows two main peaks at 1.74 Å and 2.99 Å, corresponding to the first coordination shell of Ag-C and the second coordination shell of the Ag-Ti bond, respectively. This is clear evidence that the Ag atoms in MXene-AgSAs are coordinated with C atoms. The fitting spectrum of the Ag foil, Ag_2O, and MXene-AgSAs are in

good agreement with experimental results (Figure S7 a-d and Figure S8), indicating that the fitting results are reliable. According to the EXAFS fitting results shown in Figure 1c and Table S3, the coordination number of Ag-C and Ag-Ti is 3.7 and 4.1 respectively. To further confirm that the Ag^+ ions are captured by the Ti vacancies in MXene, several pieces of evidence are provided. From the HAADF-STEM images, Ag single atoms are observed by being visually brighter than surrounding atoms. In Figure 1d, these Ag single atoms are circled in red, indicating that Ag single atoms are well-distributed in the MXene. The close-up image of an Ag single atom further confirmed that Ag atoms are implanted in MXene (Figure 1e), which is further visualized through a 3D projected image, highlighting the difference in atomic contrast between Ag single atoms and the surrounding atoms (Figure 1f).[43] The X-ray photoelectron spectroscopy (XPS) result indicates that the Ag peak appears only after introducing Ag to MXene (Figure S9) and the high-resolution XPS of Ti 2p demonstrates an increase in the oxidation state of Ti after introducing Ag, suggesting that the redox reaction between the Ti vacancies and the Ag^+ ions has occurred (Figure S10a). This is coupled with a rightward shift of the Ti-C peak near 455.5 eV to lower binding energy, indicating an elevated valence of Ti. Furthermore, the C 1s peak near the 282 eV (C-Ti bond) also demonstrates a similar shift (Figure S10b). For the charged state of Ag, the high-resolution XPS of Ag indicates the valence of Ag is between Ag^0 and Ag^+ (Figure S11). The above results indicate that the Ag atoms are captured by the Ti vacancies, influencing the charge states of Ti and C.

Besides, the wavelet transformed (WT) of the EXAFS spectrums is displayed in Figure 1i, delivering the maximum intensity at 3.5 $Å^{-1}$, which can be assigned to Ag-C coordination without Ag-Ag and Ag-O signals (Figure 1g-1h). The second coordination shell of Ag-Ti is also labelled in the wavelet-transformed EXAFS spectrum of MXene-AgSAs. Based on the above, we can deduce that the Ag single atoms are captured by the Ti vacancies and stabilized by the formation of four Ag-C bonds with four adjacent C atoms. Therefore, it can be concluded that Ag single atoms are well-dispersed in the MXene with Ag-C coordination, forming a novel MXene-AgSAs material.

To assess the effect of Ag single atoms on the Li deposition process, we compared the Li deposition morphologies on Cu, MXene, and MXene-AgSAs respectively. Based on the SEM results obtained after plating different amounts of Li, it is evident that the Li deposition is non-uniform following plating 0.2, 0.5, and 1 mAh cm^{-2} on Cu foil (Figure 2a-2c). Specifically, dendrites are observed after plating at only 4 mAh cm^{-2} (Figure 2d), while severe dendritic growth is apparent after plating at 8 mAh cm^{-2} (Figure 2e). For the MXene substrate, Li dendrites are not readily apparent after plating at 0.2, 0.5, 1, and 4 mAh cm^{-2} (Figure 2f-2i), but the distribution of the Li is still not uniform. They become pronounced after plating at 8 mAh cm^{-2} (Figure 2j). Conversely, on the MXene-AgSAs substrate, it is evident that uniform spherical Li deposition occurs after plating at 1 mAh cm^{-2} (Figure 2m). At a low plated amount of 0.2 mAh cm^{-2}, there are some obvious spherical Li formed on the surface (Figure 2k), after increasing to 0.5 mAh cm^{-2} (Figure 2l), the spherical Li becomes more prominent, and its morphology remains more uniform compared to both MXene and Cu foil. This morphology persists as smooth and flat even after plating at 4 and 8 mAh cm^{-2} (Figure 2n-2o). Furthermore, the cross-sectional views of the plated Li clearly show dendrite formation on both Cu (Figure S12 a-b) and MXene (Figure S12 c-d) substrates after depositing 4 and 8 mAh cm^{-2}, respectively. In contrast, Li plated on the MXene-AgSAs substrate forms a densely stacked layer (Figure S12 e-f). These findings indicate that MXene-AgSAs substrates effectively inhibit lithium dendrite growth. Excitingly, the electrode surface of MXene-AgSAs demonstrates consistent and uniform Li deposition, even following the deposition of significant Li capacities, ranging from 10 to 40 mAh cm^{-2} (Figure 2p-2r). Remarkably, even at a deposition capacity of 80 mAh cm^{-2}, although surface Li distribution becomes slightly uneven, no visible Li dendrites are observed (Figure 2s). Subsequently, we observed the bottom morphology of the deposited Li, and we could clearly see a large amount of spherical Li at the bottom (Figure 2t). This observation suggests a potential mechanism underlying the ability of MXene-AgSAs electrodes to facilitate the deposition of ultra-high-capacity Li. Contact angle tests are also performed to evaluate the wettability of several substrates to the electrolyte. As Figure S13 shows, the contact angle between the MXene-AgSAs

substrate and electrolyte is ~27.5°, much smaller than the MXene (~71.1°), and Cu (~110.6°), indicating the better diffusion of electrolyte in MXene-AgSAs. This result may also elucidate the more uniform deposition of Li on MXene-AgSAs electrodes. The spherical Li is keeping in good shape after loading at high capacity, indicating the ultrahigh stability of the spherical Li. This phenomenon may be attributed to the presence of unique Ag single atoms occupying the Ti vacancies (Figure 3a-3b). These Ag atoms likely rearrange the charge distribution around the Ti vacancies, thereby exerting an atomic level influence on the charge density (Figure 3c-3d). A rearranged and uniform charge distribution ensures that the electric field strength across the electrode surface remains consistent in all directions. Under these conditions, Li ions deposit at a uniform rate as they approach the electrode, promoting the formation of a spherical or nearly spherical metal layer. This uniform electric field facilitates the even distribution of the deposit, leading to the natural emergence of a spherical structure. This redistribution of the electronic near the Ag atoms further result in a low current density of the electrode and uniform macroscopic depositional morphology (Figure 3e-3f), which are supported by Density functional theory (DFT) calculations and COMSOL simulations. Conversely, according to COMSOL simulations, the Li deposition morphology on the MXene and Cu substrates becomes increasingly heterogeneous, while the charge density tends to increase (Figure S15 a-b). These results indicate that Ag atoms prevent the formation of localized high electric field regions, thereby inhibiting the growth of irregular, sharp structures like dendrites, thus promoting the formation of spherical deposits. Moreover, the presence of Ag single atoms promotes the formation of thick and stable SEI, which is thicker than the current record (~10-20 nm).[44, 45] This was supported by the Cryo-TEM image showing the thickness of the SEI to be ≈70 nm (Figure S14). The thicker SEI layer may explain why spherical Li is stabilized and maintains its shape during high-volume deposition.

To explore the composition of the thick SEI, XPS with depth profiling was employed to determine the identity of the SEI layer. Based on the XPS results in Figure 3g, the external layer of the SEI is organic, which can give flexibility to spherical Li. As the depth increases, the organic -CF_2, -(CH_2CH_2O)-, and RCH_2OCO_2Li-related peaks

disappear gradually in C 1s spectra. Furthermore, the peak intensity of Li-C (282.5 eV) increased while the intensity of the Li_2CO_3 (290 eV) decreased. The high-resolution spectra of F 1s and O 1s also show that the contents of LiF (685.5 eV) and Li_2O (529.5 eV) are higher in the inner SEI layer, while the organic -CF_3 (689 eV) contents and Li_2CO_3 (531.5 eV) salt are lower in the inner layer (Figure 3h-3i), consistent with the C 1s spectra. The increase of these inorganic salt components effectively improves Li ion conduction. The atomic ratio of the different elements also indicates that the amount of Li and F increased, but the ratio of C and O decreased (Figure 3j). This result indicates that the composition of the outer SEI layer is dominated by the organic content and Li_2CO_3, while the inner SEI membrane is dominated by inorganic salts Li_2O and LiF, with a small number of organic compounds (-CF_2, R-CH_2OCO_2Li) intercalated in the inner SEI layer. The inorganic salts in the inner SEI layer effectively ensures the fast conduction of Li ions, while the organic layer in outer SEI layer ensures the flexibility of the spherical Li.[46-48] Hence, this shows that the introduction of Ag single atoms not only guides the deposition of spherical Li metal but also catalyzes the formation of inorganic salts rich in the inner layer and thick SEI films, leading to the formation of a more stable spherical Li morphology. Besides, the binding energy (BE) is also investigated to enhance the understanding, which can also show the importance introducing of the Ag atoms in Ti vacancies. In general, electrostatic interactions between the negative sites on the anode substrate and the Li-ions in the electrolyte facilitate the driving of Li-ions to the lithiophilic sites for nucleation. The lithiophilicity of the anode can be quantified by assessing the BE between the Li and the anode. A higher BE leads to a smaller barrier to Li nucleation, resulting in a lower nucleation overpotential and smooth Li deposition.[29, 30, 49, 50] The lithiophilic property of the different bonds in the MXene-AgSAs is demonstrated by the DFT calculation. As summarized in Figure 3k and 3l, the Ag-C bond in Mxene-AgSAs is more susceptible to Li adsorption (-2.36913 eV), which indicates much stronger interaction with Li compared to Ti-C (-1.82652 eV), Ti-O (-1.50363 eV), Ti-OH (-1.36932 eV), Ti-F (-0.86912 eV), and Cu (-0.53693 eV). This result suggests that Li nucleation tends to occur at the Ag-C site, which is consistent with the reported results that lithiophilic Ag

can effectively reduce the barriers to Li nucleation and confer uniform Li deposition.[51] The lithiophilicity observed may stem from variances in the charge distribution surrounding the Ag atoms. Due to the uniform distribution of Ag single atoms in these Ti vacancies, Li ions tend to concentrate around these higher lithiophilic Ag-C sites during the Li deposition process. Hence, the spherical Li may generate from these Ag atoms due to the lithiophilic of the Ag-C sites and the uniform electronic distribution near the sites. As the plating capacity increases, the deposited Li gradually forms spherical Li near the Ag atoms, which inhibits the formation of Li dendrites and achieves a high performance of Li metal battery.

Subsequent electrochemical testing was conducted to assess the impact of Ag single atoms on the electrochemical performance. The Coulombic efficiency (CE) is a crucial parameter to evaluate the sustainability and practicality of Li metal anodes. Typical coin cells by coupling bare Li with Cu, MXene, and MXene-AgSAs are assembled to compare the CE. Figure 4a shows the relationship between CE and cell cycle number for the same plating capacity of 1 mAh cm^{-2} at a current density of 0.5 mA cm^{-2}. Compared with Cu and MXene, the MXene-AgSAs electrode delivers a more stable cycling and a longer cycle life (more than 500 cycles) with a stable CE of around 98.6%. The nucleation overpotential of MXene-AgSAs is 51 mV at 0.5 mA cm^{-2}, as shown in Figure S16, which is smaller than MXene (70 mV) and Cu (73 mV). This result indicates that the Ag single atoms modified MXene exhibits a better lithiophilic character. As the current density increases to 1 mA cm^{-2}, the MXene-AgSAs achieve a high CE of 98.0% for more than 300 cycles, while the CE of Cu and MXene dropped below 80% after 50 and 90 cycles respectively. The charge and discharge curves of different cycles for MXene-AgSAs electrodes at current densities of 0.5 mA cm^{-2} and 1 mA cm^{-2} also show that MXene-AgSAs electrodes have a smaller hysteresis voltage (Figure S17). On the contrary, the charge and discharge curves of MXene (Figure S18) and Cu (Figure S19) deliver an increasing hysteresis voltage at current densities of 0.5 mA cm^{-2} and 1 mA cm^{-2}. In further experiments, the MXene-AgSAs anode shows an ultra-stable and high CE over 98% at 0.5 mA cm^{-2} with a capacity of 0.5 mAh cm^{-2} for more than 800 cycles (Figure S20), indicating the Ag single atoms have an excellent

ability to inhibit the growth of dendrites. To investigate the status of dendrites during cycling, SEM is conducted after different cycles. As shown in Figure S21, dendrites are formed on the Cu foil surface after 10 cycles at 1 mA cm^{-2} with a capacity of 1 mAh cm^{-2}, which becomes more serious after 50 cycles, with dead Li growth on the surface at the same time. For the MXene, a flat morphology is observed after 10 cycles, but dendrites are formed after 50 cycles, indicating the weak dendritic inhibition property. Nonetheless, the MXene-AgSAs electrode shows excellent ability to suppress the dendrites growth. MXene-AgSAs deliver a smooth surface after cycling, indicating their great ability to inhibit Li dendrites. In addition, the MXene-AgSAs also exhibit good stability and reusability. Figure S22 shows the HAADF-STEM and EDS mapping image of the MXene-AgSAs after 10 cycles at 0.5 mA cm^{-2} with 1 mAh cm^{-2} the atomic dispersion of Ag atoms is well retained, indicating the good stability of the Ag atoms in the electrode.

To investigate the interfacial stability and Li-ion transport capabilities, we plated Li on MXene-AgSAs to obtain an anode (MXene-AgSAs@Li) with a capacity of 5 mAh cm^{-2} and assembled a symmetric cell of MXene-AgSAs@Li/Li. The morphology of the MXene-AgSAs@Li after plating 5 mAh cm^{-2} is shown in Figure S23, in which the thickness of the plated Li is about 15 μm. MXene@Li and Cu@Li electrodes are prepared with the same method. The rate cycling performance of the symmetric cell is shown in Figure 4c, in which the long-term overpotential of MXene-AgSAs delivers a smaller and more stable voltage hysteresis during the switch of different current densities from 0.5 mA cm^{-2} to 8 mA cm^{-2} with a capacity of 1 mAh cm^{-2}. In comparison, the MXene and Cu electrodes show a larger voltage hysteresis during the switch of current densities. Figures 4d and 4e exhibit the voltage profile of symmetrical cells at the current density of 2 mA cm^{-2} and 1 mA cm^{-2} with the capacity of 1 mAh cm^{-2} and 2 mAh cm^{-2} respectively. It shows that the MXene-AgSAs electrode exhibits a flat Li stripping/plating plateau with a small voltage hysteresis (~ 40 mV) beyond 400 hours at the current density of 2 mA cm^{-2} with the capacity of 1 mAh cm^{-2}. However, the Cu and MXene electrodes show an increasing voltage hysteresis after cycling for about 90 hours and 120 hours respectively. At 1 mA cm^{-2} with a capacity of 2 mAh cm^{-2}, the

MXene-AgSAs electrode also shows a stable performance for more than 500 hours. In comparison, the voltage hysteresis of Cu and MXene electrodes increased and became unstable after 200 and 300 hours respectively. To test the superior modulation of Li deposition by MXene-AgSAs, the plating and striping capacity increased to 10 mAh cm^{-2} and 40 mAh cm^{-2} at 1 mA cm^{-2} respectively (Figure 4f and 4g), and the MXene-AgSAs electrode still shows a stable cycling performance over 800 hours. The highly stable cycle life and low voltage hysteresis of the symmetrical cell indicate that the MXene-AgSAs@Li anode can operate under practical cycling conditions. To compare the charge transfer kinetics of the MXene-AgSAs@Li with MXene@Li and Cu@Li, the exchange current densities are calculated and compared via Tafel plots (Figure 4h). The MXene-AgSAs@Li electrode exhibited an exchange current density of 2.06 mA cm^{-2}, which is significantly higher than that of MXene@Li (0.359 mA cm^{-2}) as well as Cu@Li (0.172 mA cm^{-2}). This substantially higher exchange current density of the MXene-AgSAs@Li electrode reflects the enhanced electrochemical reaction kinetics of the MXene-AgSAs@Li electrode, indicating a lower Li nucleation barrier and overpotential during Li plating/stripping. Meanwhile, the incorporation of Ag single atoms enhanced the ion and electron transfer kinetics. To verify that MXene-AgSAs improve the reaction kinetics of the electrodes, EIS measurements were carried out in the half-symmetric cells of MXene-AgSAs, MXene, and Cu. As shown in Figures 4i and 4j, the MXene-AgSAs electrode exhibits a smaller impedance of about 18 and 13 Ω after 10 and 50 cycles at 1 mA cm^{-2} and 1 mAh cm^{-2}. However, MXene and Cu electrodes display a larger and increasing impedance after different cycles. This phenomenon supports the superiority of MXene-AgSAs electrodes in stabilizing the inter-reactive phase of Li/electrolyte and enhancing the transport of Li^+ ions over the formed SEI. Thus, our work demonstrates superior performance compared to some other reported studies, as outlined in Figure 4k and Table S4.

To demonstrate the application potential of MXene-AgSAs@Li as an anode for Li-ion and Li-sulfur batteries, full cells are assembled MXene-AgSAs@Li with $LiFePO_4$ and S cathodes respectively. As a comparison, a full cell using a bare Li anode is also assembled with the same cathode. As illustrated in Figure 5a, the MXene-

AgSAs@Li||$LiFePO_4$ full cell shows a higher initial capacity of 150 mAh g^{-1} and a more stable capacity retention of 126 mAh g^{-1} (84.36%) after 400 cycles. However, the full cell of bare Li could only provide 63.16% capacity retention at 1 C, indicating rapid capacity decay. Figure 5b shows MXene-AgSAs@Li||S full cell delivers a more stable and long cycle life at 2 C, which maintains 200 mAh g^{-1} after 1000 cycles. However, the bare Li||S full cell shows a decreasing capacity and only delivers a capacity of 100 mAh g^{-1} after 1000 cycles. Figure 5c shows that the rate performance of the MXene-AgSAs@Li||$LiFePO_4$ is much better than that of bare Li anodes at different current densities. The capacity of the full cell with bare Li drops sharply and approaches zero at 5C. In contrast, the MXene-AgSAs@Li||$LiFePO_4$ still has a high reversible capacity of 103 mAh g^{-1} at 5C. The charge/discharge curves of MXene-AgSAs@Li for different current densities at 0.2, 0.5, 1, 2, 3, 4, and 5C are shown in Figure 5d. Its polarization voltage is smaller than that of bare Li (Figure S24a). Additionally, the MXene-AgSAs@Li||S full cell also shows a better rate performance than bare Li high current densities (Figure 5e and Figure S24b). These two results indicate that the MXene-AgSAs@Li electrodes have good potential in practical applications.

In summary, by introducing Ag single atoms into the vacancies of MXene, we successfully facilitated the formation of stable and uniform spherical Li, effectively inhibiting Li dendrite growth. We discussed and verified the effect of Ag single atoms on Li nucleation, spherical Li growth, and charge distribution. Based on our studies, we could conclude that the Ag single atoms enabled the regulation of charge distribution around the original Ti vacancies, thus affecting the Li^+-ion deposition concentration and the shape of the deposited. Benefiting from these advantages, a high CE of over 98% can be achieved at a current density of 0.5 mA cm^{-2} with a capacity of 0.5 mAh cm^{-2} for more than 800 cycles. Symmetric cells are also plated and stripped with an ultra-high capacity of up to 40 mAh cm^{-2} and cycled stably for more than 800 hours. Full cells assembled using MXene-AgSAs@Li anodes paired with $LiFePO_4$ cathodes or S cathodes individually exhibit enhanced cycling and rate performances. These findings underscore the significance of a high-quality anode in practical battery

applications. Consequently, these remarkable properties effectively suppress Li dendrite formation, offering promising prospects for the practical integration of noble metals in Li metal batteries. We anticipate that this study will inspire novel approaches for Li anode design and enhance our comprehension of Li nucleation principles.

Author contributions

X. L. Li conceived idea and conducted the data collection and analysis. W.Y. Lieu and L. Wang assisted with the synthesis of MXene and reviewed the paper. D. Yan, and Y. Li assisted with synchrotron data fitting. T. G, and Y. Li assisted in the test of the material. J. Lu, Z.W. Seh, and H.Y. Yang supervised the project and wrote the manuscript.

Supporting Information

Detailed experimental procedures and additional figures and tables. Figures of SEM images, XRD patterns, TEM and HAADF-STEM images, XPS spectra, Cryo-TEM spectra, EXAFS and fitting spectra, COMSOL simulation results, electrochemical performances of Coulombic efficiencies and voltage hysteresis, performance of full cell, metal price comparison table, Ag loading ratio table, EXAFS fitting table and performance comparison table.

Acknowledgments

This work is supported by the Singapore Ministry of Education academic research grant Tier 2 (T2EP50121-0007) and the Agency for Science, Technology and Research (Central Research Fund Award).

Competing interests

The authors declare no competing interests.

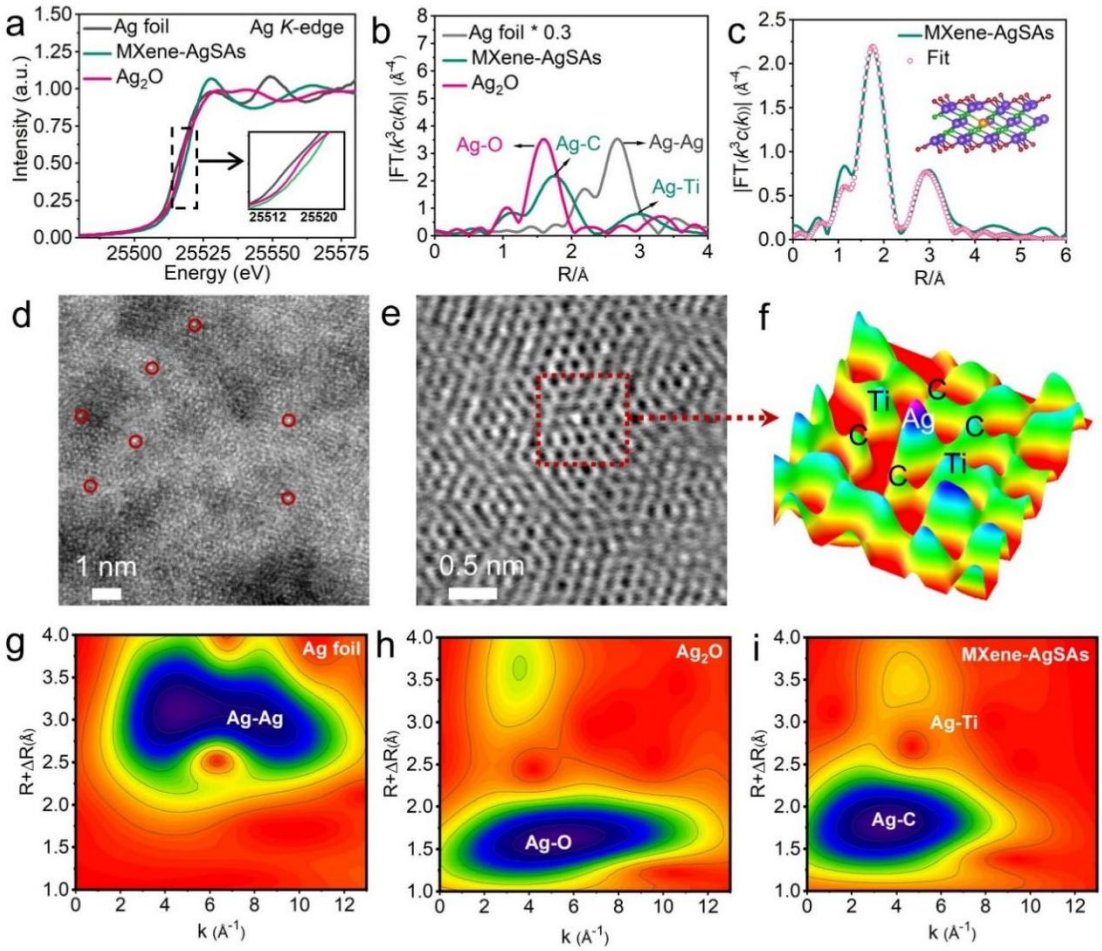

Figure 1. (a) XANES spectra at the Ag K-edge; (b) the K^3-weighted Fourier transforms of Ag K-edge EXAFS spectra for MXene-AgSAs, Ag foil, and Ag_2O; (c) the K^3-weighted Fourier transforms of Ag K-edge EXAFS spectra for MXene-AgSAs and fitting line; (d) HAADF-STEM image of Ag single atoms on MXene; (e) HAADF-STEM image of Ag single atoms in MXene lattice; (f) the 3D atom distribution and morphology of the labelled area; wavelet transformed Ag K-edge EXAFS spectra for Ag foil (g), Ag_2O (h) , and MXene-AgSA (i).

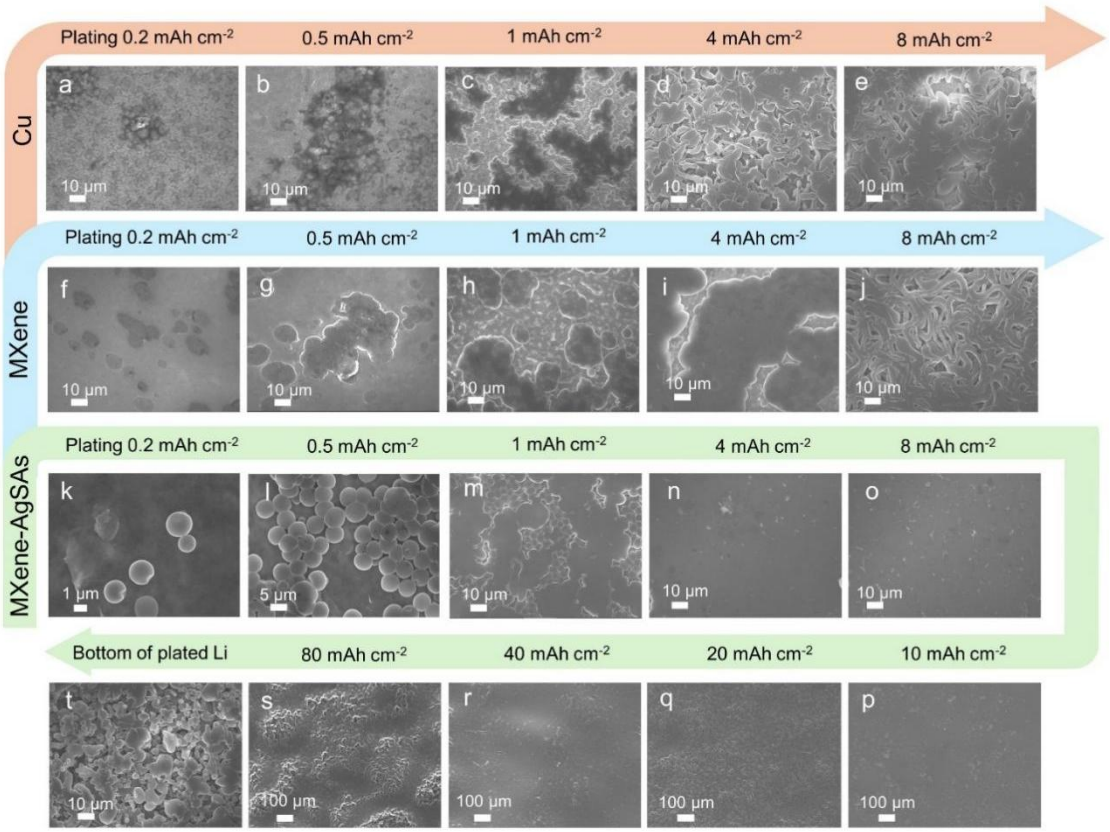

Figure 2. The morphologies of the Cu (a-e), MXene (f-j), and MXene-AgSAs (k-o) after plating 0.2, 0.5, 1, 4, and 8 mAh cm^{-2}; (f-j) the morphologies of MXene-AgSAs after plating 10, 20, 40, 80 mAh cm^{-2} (p-s), and (t) the bottom morphology of the Li after plating 80 mAh cm^{-2}.

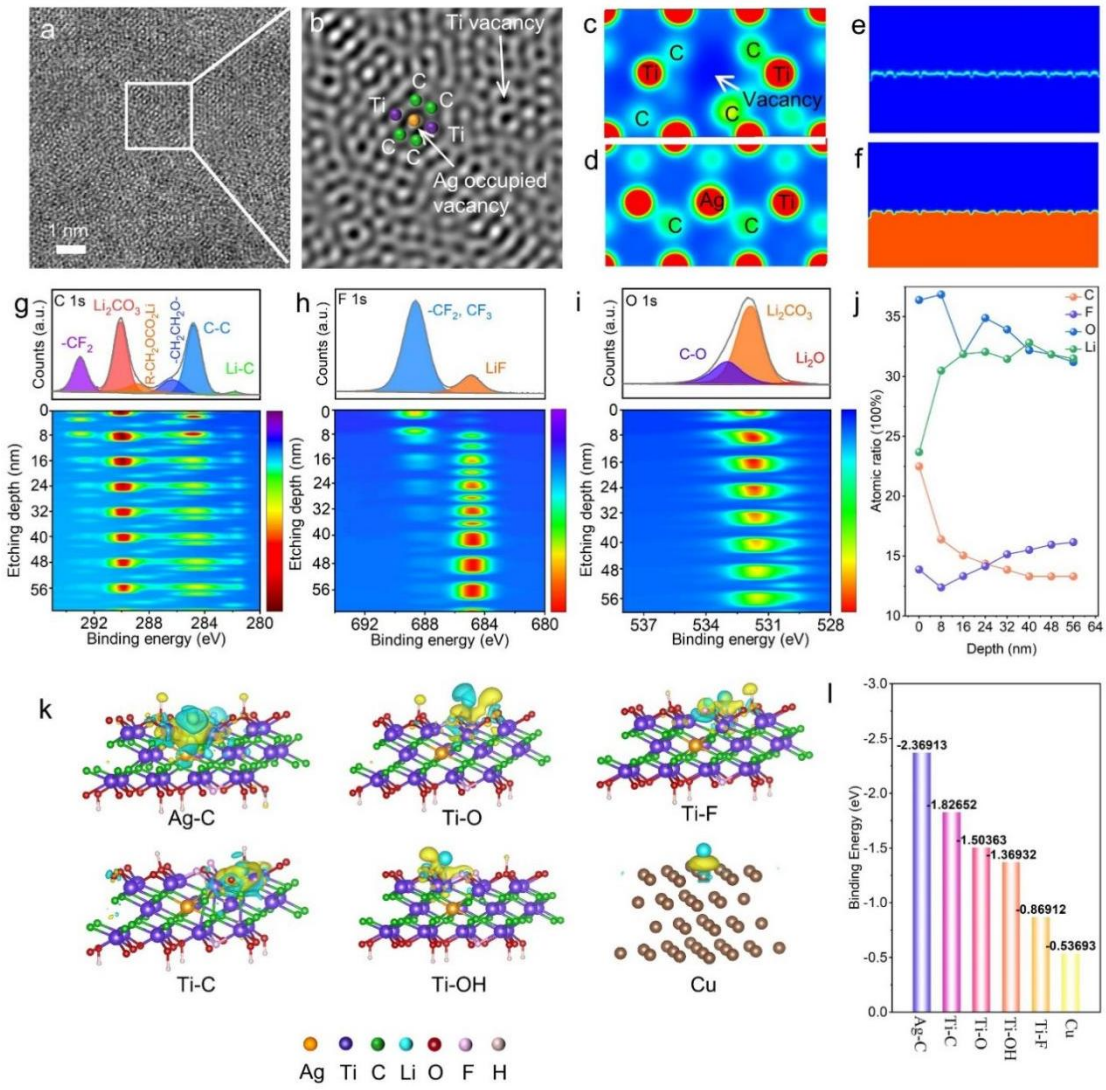

Figure 3. (a) The HAADF-STEM of MXene-AgSAs and the vacancies occupied by Ag atoms (b); The calculated electron charge density distribution near the vacancies of MXene (c) and MXene-AgSAs (d); 2D phase-field simulation of local current density distribution on MXene-AgSAs (e) and Li deposition morphology (f); C 1s (g), F 1s (h), and O 1s (i) in-depth XPS spectra of SEI layer on MXene-AgSAs@Li; (j) the atomic ratio of different element at different etching depth; (k) Differential charge density between Li and the related bonds in MXene-AgSAs; (l) Summary of the calculated binding energy of Li with different bond in the MXene-AgSAs composites.

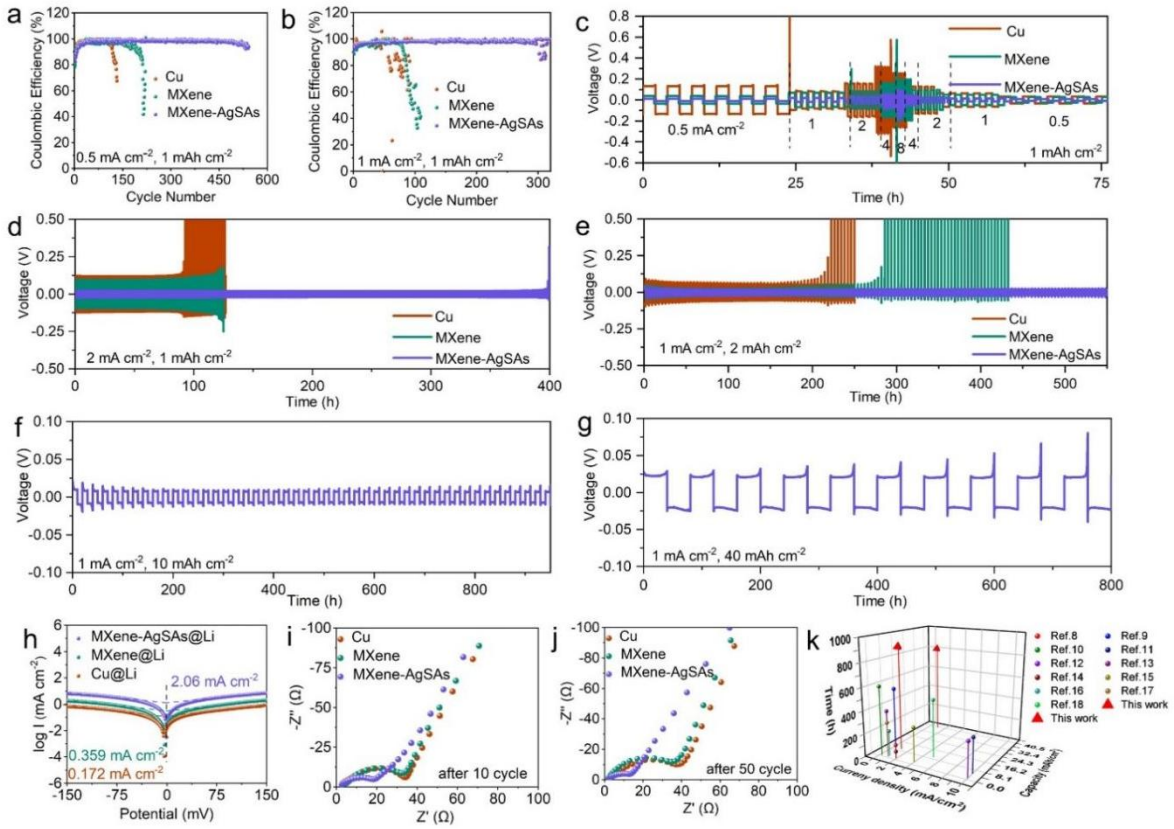

Figure 4. CE of Li deposition on Cu, MXene, and MXene-AgSAs at a current density of 0.5 mA cm^{-2} (a) and 1 mA cm^{-2} (b) with a deposition capacity of 1 mAh cm^{-2}; (c) the rating performance of Cu, MXene, and MXene-AgSAs at a current density of 0.5, 1, 2, 4, 8, 4, 2, 1, and 0.5 mA cm^{-2} with a deposition capacity of 1 mAh cm^{-2}; (d) the cycling performance of Cu, MXene, and MXene-AgSAs at a current density of 2 mA cm^{-2} with a deposition capacity of 1 mAh cm^{-2}; (e) the cycling performance of Cu, MXene, and MXene-AgSAs at a current density of 1 mA cm^{-2} with a deposition capacity of 2 mAh cm^{-2}; (f) the cycling performance of MXene-AgSAs at a current density of 1 mA cm^{-2} and a deposition capacity of 10 mAh cm^{-2} and 40 mAh cm^{-2} (g); (h) Tafel curves of MXene-AgSAs@Li, MXene@Li , and Cu@Li symmetric cells; Impedance spectra of Cu, MXene, and MXene-AgSAs half-symmetric cells after 10 cycles (i) and 50 cycles (j) at 1 mA cm^{-2} and 1 mAh cm^{-2}.

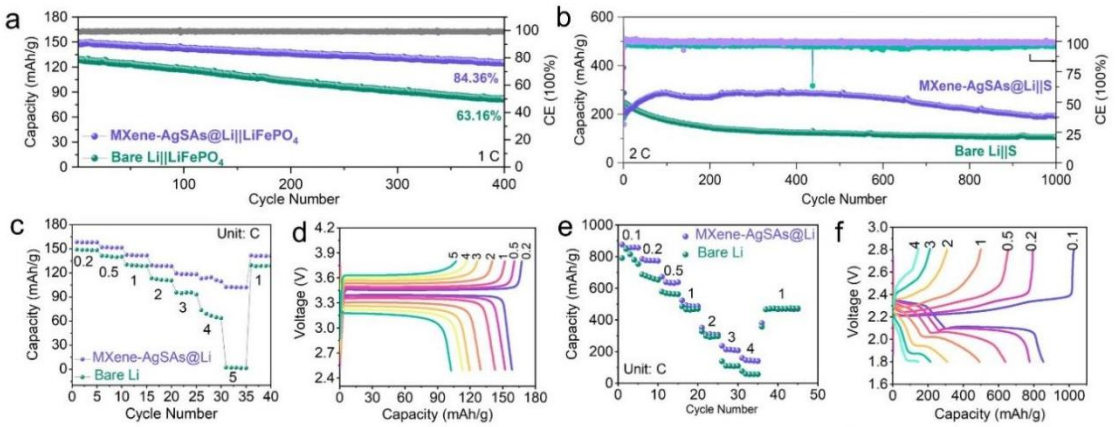

Figure 5. (a) Cycling performance of MXene-AgSAs@Li/$LiFePO_4$ and bare Li/$LiFePO_4$ at 1C; (b) Cycling performance of MXene-AgSAs@Li/S and bare Li/S at 2C; (c) Rate capabilities of MXene-AgSAs@Li/$LiFePO_4$ and bare Li/$LiFePO_4$ at various current densities from 0.2 C to 5 C and related charge and discharge curves (d); (e) Rate capabilities of MXene-AgSAs@Li/S and bare Li/S at various current density from 0.1 C to 4 C and related selected charge and discharge curves (f).

References:

(1) Zhu, H. L.; Luo, W.; Ciesielski, P. N.; Fang, Z. Q.; Zhu, J. Y.; Henriksson, G.; Himmel, M. E.; Hu, L. B. Wood-Derived Materials for Green Electronics, Biological Devices, and Energy Applications. *Chem. Rev.* **2016**, *116* (16), 9305-9374. DOI: 10.1021/acs.chemrev.6b00225.

(2) Mackanic, D. G.; Chang, T. H.; Huang, Z. J.; Cui, Y.; Bao, Z. N. Stretchable electrochemical energy storage devices. *Chem. Soc. Rev.* **2020**, *49* (13), 4466-4495. DOI: 10.1039/d0cs00035c.

(3) Al Shaqsi, A. Z.; Sopian, K.; Al-Hinai, A. Review of energy storage services, applications, limitations, and benefits. *Energy Reports* **2020**, *6*, 288-306. DOI: 10.1016/j.egyr.2020.07.028.

(4) Liu, K.; Liu, Y. Y.; Lin, D. C.; Pei, A.; Cui, Y. Materials for lithium-ion battery safety. *Sci. Adv.* **2018**, *4* (6). DOI: 10.1126/sciadv.aas9820.

(5) Duffner, F.; Kronemeyer, N.; Tubke, J.; Leker, J.; Winter, M.; Schmuch, R. Post-lithium-ion battery cell production and its compatibility with lithium-ion cell production infrastructure. *Nat. Energy.* **2021**, *6* (2), 123-134. DOI: 10.1038/s41560-020-00748-8.

(6) Weiss, M.; Ruess, R.; Kasnatscheew, J.; Levartovsky, Y.; Levy, N. R.; Minnmann, P.; Stolz, L.; Waldmann, T.; Wohlfahrt-Mehrens, M.; Aurbach, D.; et al. Fast Charging of Lithium-Ion Batteries: A Review of Materials Aspects. *Adv. Energy Mater.* **2021**, *11* (33), 2101126. DOI: 10.1002/aenm.202101126.

(7) Sun, J. L.; Xu, Y. F.; Lv, Y. Q.; Zhang, Q. C.; Zhou, X. S. Recent Advances in Covalent Organic Framework Electrode Materials for Alkali Metal-Ion Batteries. *CCS Chem.* **2023**, *5* (6), 1259-1276. DOI: 10.31635/ccschem.023.202302808.

(8) Wang, H.; Yao, C. J.; Nie, H. J.; Wang, K. Z.; Zhong, Y. W.; Chen, P. W.; Mei, S. L.; Zhang, Q. C. Recent progress in carbonyl-based organic polymers as promising electrode materials for lithium-ion batteries (LIBs). *J. Mater. Chem.* **2020**, *8* (24), 11906-11922. DOI: 10.1039/d0ta03321a.

(9) Niu, C. J.; Pan, H. L.; Xu, W.; Xiao, J.; Zhang, J. G.; Luo, L. L.; Wang, C. M.; Mei, D. H.; Meng, J. S.; Wang, X. P.; et al. Self-smoothing anode for achieving high-energy lithium metal batteries under realistic conditions. *Nat. Nanotechnol.* **2019**, *14* (6), 594-+. DOI: 10.1038/s41565-019-0427-9.

(10) Liu, J.; Bao, Z. N.; Cui, Y.; Dufek, E. J.; Goodenough, J. B.; Khalifah, P.; Li, Q. Y.; Liaw, B. Y.; Liu, P.; Manthiram, A.; et al. Pathways for practical high-energy long-cycling lithium metal batteries. *Nat. Energy.* **2019**, *4* (3), 180-186. DOI: 10.1038/s41560-019-0338-x.

(11) Chen, X. R.; Zhao, B. C.; Yan, C.; Zhang, Q. Review on Li Deposition in Working Batteries: From Nucleation to Early Growth. *Adv. Mater.* **2021**, *33* (8), 2004128. DOI: 10.1002/adma.202004128.

(12) Seh, Z. W.; Sun, Y. M.; Zhang, Q. F.; Cui, Y. Designing high-energy lithium-sulfur batteries. *Chem. Soc. Rev.* **2016**, *45* (20), 5605-5634. DOI: 10.1039/c5cs00410a.

(13) Chen, K.; Yang, D. Y.; Huang, G.; Zhang, X. B. Lithium-Air Batteries: Air-Electrochemistry and Anode Stabilization. *Acc. Chem. Res.* **2021**, *54* (3), 632-641. DOI: 10.1021/acs.accounts.0c00772.

(14) Aurbach, D.; McCloskey, B. D.; Nazar, L. F.; Bruce, P. G. Advances in understanding mechanisms underpinning lithium-air batteries. *Nat. Energy.* **2016**, *1,* 16128. DOI: 10.1038/nenergy.2016.128.

(15) Liu, Y. Y.; Lin, D. C.; Jin, Y.; Liu, K.; Tao, X. Y.; Zhang, Q. H.; Zhang, X. K.; Cui, Y. Transforming from planar to three-dimensional lithium with flowable interphase for solid lithium metal batteries. *Sci. Adv.* **2017**, *3* (10), eaao0713. DOI: 10.1126/sciadv.aao0713.
(16) Yan, D.; Yang, H. Y.; Bai, Y. Tactics to optimize conversion-type metal fluoride/sulfide/oxide cathodes toward advanced lithium metal batteries. *Nano Res.* **2023**, *16* (6), 8173-8190. DOI: 10.1007/s12274-023-5427-7.
(17) Meyerson, M. L.; Papa, P. E.; Heller, A.; Mullins, C. B. Recent Developments in Dendrite-Free Lithium-Metal Deposition through Tailoring of Micro- and Nanoscale Artificial Coatings. *Acs Nano* **2021**, *15* (1), 29-46. DOI: 10.1021/acsnano.0c05636.
(18) Zhang, X. Y.; Wang, A. X.; Liu, X. J.; Luo, J. Y. Dendrites in Lithium Metal Anodes: Suppression, Regulation, and Elimination. *Acc. Chem. Res.* **2019**, *52* (11), 3223-3232. DOI: 10.1021/acs.accounts.9b00437.
(19) Wang, X.; Zeng, W.; Hong, L.; Xu, W. W.; Yang, H. K.; Wang, F.; Duan, H. G.; Tang, M.; Jiang, H. Q. Stress-driven lithium dendrite growth mechanism and dendrite mitigation by electroplating on soft substrates. *Nat. Energy.* **2018**, *3* (3), 227-235. DOI: 10.1038/s41560-018-0104-5.
(20) Cao, D. X.; Sun, X.; Li, Q.; Natan, A.; Xiang, P. Y.; Zhu, H. L. Lithium Dendrite in All-Solid-State Batteries: Growth Mechanisms, Suppression Strategies, and Characterizations. *Matter* **2020**, *3* (1), 57-94. DOI: 10.1016/j.matt.2020.03.015.
(21) Lin, D. C.; Liu, Y. Y.; Liang, Z.; Lee, H. W.; Sun, J.; Wang, H. T.; Yan, K.; Xie, J.; Cui, Y. Layered reduced graphene oxide with nanoscale interlayer gaps as a stable host for lithium metal anodes. *Nat. Nanotechnol.* **2016**, *11* (7), 626-+. DOI: 10.1038/nnano.2016.32.
(22) Xiao, J. How lithium dendrites form in liquid batteries. *Science* **2019**, *366* (6464), 426-427. DOI: 10.1126/science.aay8672.
(23) Zhang, Y.; Zuo, T. T.; Popovic, J.; Lim, K.; Yin, Y. X.; Maier, J.; Guo, Y. G. Towards better Li metal anodes: Challenges and strategies. *Mater. Today* **2020**, *33*, 56-74. DOI: 10.1016/j.mattod.2019.09.018.
(24) Lin, D. C.; Liu, Y. Y.; Cui, Y. Reviving the lithium metal anode for high-energy batteries. *Nat. Nanotechnol.* **2017**, *12* (3), 194-206. DOI: 10.1038/nnano.2017.16.
(25) Zhang, L.; Yang, T.; Du, C.; Liu, Q.; Tang, Y.; Zhao, J.; Wang, B.; Chen, T.; Sun, Y.; Jia, P.; et al. Lithium whisker growth and stress generation in an in situ atomic force microscope-environmental transmission electron microscope set-up. *Nat. Nanotechnol.* **2020**, *15* (2), 94-98. DOI: 10.1038/s41565-019-0604-x.
(26) Jin, S.; Ye, Y. D.; Niu, Y. J.; Xu, Y. S.; Jin, H. C.; Wang, J. X.; Sun, Z. W.; Cao, A. M.; Wu, X. J.; Luo, Y.; et al. Solid-Solution-Based Metal Alloy Phase for Highly Reversible Lithium Metal Anode. *J. Am. Chem. Soc.* **2020**, *142* (19), 8818-8826. DOI: 10.1021/jacs.0c01811.
(27) Zhang, Q. K.; Zhang, X. Q.; Wan, J.; Yao, N.; Song, T. L.; Xie, J.; Hou, L. P.; Zhou, M. Y.; Chen, X.; Li, B. Q.; et al. Homogeneous and mechanically stable solid-electrolyte interphase enabled by trioxane-modulated electrolytes for lithium metal batteries. *Nat. Energy.* **2023**, *8* (7), 725-735. DOI: 10.1038/s41560-023-01275-y.
(28) Wagner-Henke, J.; Kuai, D. C.; Gerasimov, M.; Röder, F.; Balbuena, P. B.; Krewer, U. Knowledge-driven design of solid-electrolyte interphases on lithium metal via multiscale modelling. *Nat. Commun.* **2023**, *14* (1), 6823. DOI: 10.1038/s41467-023-42212-7.

(29) Yan, K.; Lu, Z. D.; Lee, H. W.; Xiong, F.; Hsu, P. C.; Li, Y. Z.; Zhao, J.; Chu, S.; Cui, Y. Selective deposition and stable encapsulation of lithium through heterogeneous seeded growth. *Nat. Energy.* **2016**, *1,* 16010. DOI: 10.1038/nenergy.2016.10.
(30) Fang, Y. J.; Zhang, S. L.; Wu, Z. P.; Luan, D. Y.; Lou, X. W. A highly stable lithium metal anode enabled by Ag nanoparticle-embedded nitrogen-doped carbon macroporous fibers. *Sci. Adv.* **2021**, *7* (21), eabg3626. DOI: 10.1126/sciadv.abg3626.
(31) Pei, A.; Zheng, G. Y.; Shi, F. F.; Li, Y. Z.; Cui, Y. Nanoscale Nucleation and Growth of Electrodeposited Lithium Metal. *Nano Lett.* **2017**, *17* (2), 1132-1139. DOI: 10.1021/acs.nanolett.6b04755.
(32) Wang, Y. Y.; Wang, Z. J.; Lei, D. N.; Lv, W.; Zhao, Q.; Ni, B.; Liu, Y.; Li, B. H.; Kang, F. Y.; He, Y. B. Spherical Li Deposited inside 3D Cu Skeleton as Anode with Ultrastable Performance. *ACS Appl. Mater. Interfaces.* **2018**, *10* (24), 20244-20249. DOI: 10.1021/acsami.8b04881.
(33) Zhou, S. Q.; Zhao, Y. X.; Shi, R.; Wang, Y. C.; Ashok, A.; Heraly, F.; Zhang, T. R.; Yuan, J. Y. Vacancy-Rich MXene-Immobilized Ni Single Atoms as a High-Performance Electrocatalyst for the Hydrazine Oxidation Reaction. *Adv. Mater.* **2022**, *34* (36), 2204388. DOI: 10.1002/adma.202204388.
(34) Zhao, D.; Chen, Z.; Yang, W. J.; Liu, S. J.; Zhang, X.; Yu, Y.; Cheong, W. C.; Zheng, L. R.; Ren, F. Q.; Ying, G. B.; et al. MXene (Ti3C2) Vacancy-Confined Single-Atom Catalyst for Efficient Functionalization of CO2. *J. Am. Chem. Soc.* **2019**, *141* (9), 4086-4093. DOI: 10.1021/jacs.8b13579.
(35) Bao, H. H.; Qiu, Y.; Peng, X. Y.; Wang, J. A.; Mi, Y. Y.; Zhao, S. Z.; Liu, X. J.; Liu, Y. F.; Cao, R.; Zhuo, L. C.; et al. Isolated copper single sites for high-performance electroreduction of carbon monoxide to multicarbon products. *Nat. Commun.* **2021**, *12* (1), 238. DOI: 10.1038/s41467-020-20336-4.
(36) Zhang, N. Q.; Zhang, X. X.; Tao, L.; Jiang, P.; Ye, C. L.; Lin, R.; Huang, Z. W.; Li, A.; Pang, D. W.; Yan, H.; et al. Silver Single-Atom Catalyst for Efficient Electrochemical CO2 Reduction Synthesized from Thermal Transformation and Surface Reconstruction. *Angew. Chem. Int. Ed.* **2021**, *60* (11), 6170-6176. DOI: 10.1002/anie.202014718.
(37) Jiang, X. H.; Zhang, L. S.; Liu, H. Y.; Wu, D. S.; Wu, F. Y.; Tian, L.; Liu, L. L.; Zou, J. P.; Luo, S. L.; Chen, B. B. Silver Single Atom in Carbon Nitride Catalyst for Highly Efficient Photocatalytic Hydrogen Evolution. *Angew. Chem. Int. Ed.* **2020**, *59* (51), 23112-23116. DOI: 10.1002/anie.202011495.
(38) Lim, K. R. G.; Shekhirev, M.; Wyatt, B. C.; Anasori, B.; Gogotsi, Y.; Seh, Z. W. Fundamentals of MXene synthesis. *Nat. Synth.* **2022**, *1* (8), 601-614. DOI: 10.1038/s44160-022-00104-6.
(39) Shi, H. D.; Zhang, C. J.; Lu, P. F.; Dong, Y. F.; Wen, P. C.; Wu, Z. S. Conducting and Lithiophilic MXene/Graphene Framework for High-Capacity, Dendrite-Free Lithium-Metal Anodes. *ACS Nano* **2019**, *13* (12), 14308-14318. DOI: 10.1021/acsnano.9b07710.
(40) Zhang, X. Y.; Lv, R. J.; Wang, A. X.; Guo, W. Q.; Liu, X. J.; Luo, J. Y. MXene Aerogel Scaffolds for High-Rate Lithium Metal Anodes. *Angew. Chem. Int. Ed.* **2018**, *57* (46), 15028-15033. DOI: 10.1002/anie.201808714.
(41) Naguib, M.; Kurtoglu, M.; Presser, V.; Lu, J.; Niu, J. J.; Heon, M.; Hultman, L.; Gogotsi, Y.; Barsoum, M. W. Two-Dimensional Nanocrystals Produced by Exfoliation of Ti3AlC2. *Adv. Mater.* **2011**, *23* (37), 4248-4253. DOI: 10.1002/adma.201102306.

(42) Cao, Z. J.; Zhu, Q.; Wang, S.; Zhang, D.; Chen, H.; Du, Z. G.; Li, B.; Yang, S. B. Perpendicular MXene Arrays with Periodic Interspaces toward Dendrite-Free Lithium Metal Anodes with High-Rate Capabilities. *Adv. Funct. Mater.* **2020**, *30* (5), 1908075. DOI: 10.1002/adfm.201908075.
(43) Chen, Y. X.; Kasama, T.; Huang, Z. W.; Hu, P. P.; Chen, J. M.; Liu, X.; Tang, X. F. Highly Dense Isolated Metal Atom Catalytic Sites: Dynamic Formation and In Situ Observations. *Chem. Eur. J.* **2015**, *21* (48), 17397-17402. DOI: 10.1002/chem.201503068.
(44) Liu, Y. Y.; Lin, D. C.; Li, Y. Z.; Chen, G. X.; Pei, A.; Nix, O.; Li, Y. B.; Cui, Y. Solubility-mediated sustained release enabling nitrate additive in carbonate electrolytes for stable lithium metal anode. *Nat. Commun.* **2018**, *9,* 3656. DOI: 10.1038/s41467-018-06077-5.
(45) Wu, H. P.; Jia, H.; Wang, C. M.; Zhang, J. G.; Xu, W. Recent Progress in Understanding Solid Electrolyte Interphase on Lithium Metal Anodes. *Adv. Energy Mater.* **2021**, *11* (5), 2003092. DOI: 10.1002/aenm.202003092.
(46) Li, Y. Z.; Li, Y. B.; Pei, A. L.; Yan, K.; Sun, Y. M.; Wu, C. L.; Joubert, L. M.; Chin, R.; Koh, A. L.; Yu, Y.; et al. Atomic structure of sensitive battery materials and Interfaces revealed by cryo-electron microscopy. *Science* **2017**, *358* (6362), 506-510. DOI: 10.1126/science.aam6014.
(47) Wi, T. U.; Park, S. O.; Yeom, S. J.; Kim, M. H.; Kristanto, I.; Wang, H. T.; Kwak, S. K.; Lee, H. W. Revealing the Dual-Layered Solid Electrolyte Interphase on Lithium Metal Anodes via Cryogenic Electron Microscopy. *ACS Energy Lett.* **2023**, *8* (5), 2193-2200. DOI: 10.1021/acsenergylett.3c00505.
(48) Yu, W. L.; Yu, Z. A.; Cui, Y.; Bao, Z. A. Degradation and Speciation of Li Salts during XPS Analysis for Battery Research. *ACS Energy Lett.* **2022**, *7* (10), 3270-3275. DOI: 10.1021/acsenergylett.2c01587.
(49) Chen, X.; Chen, X. R.; Hou, T. Z.; Li, B. Q.; Cheng, X. B.; Zhang, R.; Zhang, Q. Lithiophilicity chemistry of heteroatom-doped carbon to guide uniform lithium nucleation in lithium metal anodes. *Sci. Adv.* **2019**, *5* (2), eaau7728. DOI: 10.1126/sciadv.aau7728.
(50) Zhang, W. D.; Zhuang, H. L. L.; Fan, L.; Gao, L. N.; Lu, Y. Y. A "cation-anion regulation" synergistic anode host for dendrite-free lithium metal batteries. *Sci. Adv.* **2018**, *4* (2), eaar4410. DOI: 10.1126/sciadv.aar4410.
(51) Li, X. L.; Huang, S. Z.; Yan, D.; Zhang, J.; Fang, D. L.; Von Lim, Y.; Wang, Y.; Li, T. C.; Li, Y. F.; Guo, L.; et al. Tuning Lithiophilicity and Stability of 3D Conductive Scaffold via Covalent Ag-S Bond for High-Performance Lithium Metal Anode. *Energy Environ. Mater.* **2023***, 6,* e12274. DOI: 10.1002/eem2.12274.